



Cite this: *RSC Adv.*, 2023, 13, 23409

Double cross-linked transparent superhydrophilic coating capable of anti-fogging even after abrasion and boiling†

Xingyu Liu,^a Lili Xu,^a Shuaisheng Zhao,^{*a} Haoxuan Hua,^a Yifan Su,^a Xinquan Yu,^a Jinlei Wang,^b Gang Li^b and Youfa Zhang[†]  ^{*a}

The commercial application of surfaces with superhydrophilic (SHPL) properties is well known as an efficient strategy to address problems such as anti-fogging, anti-frosting, and anti-biological contamination. However, current SHPL coatings are limited by their poor water and abrasion resistances. Thus, herein, to solve these problems active glass was employed as a substrate, and a stable and transparent SHPL solution was prepared *via* the spraying process. Aqueous polyacrylic resin (PAA), SiO₂ nanoparticles (NPs), tetraethyl orthosilicate (TEOS), and sodium allyl sulfonate (SDS) were utilized as the four main components of the PAA-TEOS-SiO₂ coating. The durability properties including anti-abrasion, resistance to water, and contact component loss were investigated *via* the Taber abrasion test, boiling water immersion test, and anti-fogging test, respectively. Furthermore, the structure, composition, and wettability of the coating before and after the friction and water immersion tests were compared *via* water contact angle (WCA) measurements. Furthermore, the effect of the type of resin on the properties of the coating was investigated. The surface morphology of the blended water-based polyacrylic acid (PAA) resin was uniform and flat and its adhesion to the substrate was the highest (4.21 MPa). Considering the durability and optical properties of the coating, the optimal blend was 3 wt% PAA resin, which exhibited a transmittance of 90%. When the content of TEOS, which enhanced the crosslinking in the coating, was increased to 2 wt%, the results showed that the SHPL coating maintained good anti-friction, boiling resistance, and anti-fogging properties under the conditions of 300 cycle Taber friction with 250 g load and soaking in hot water at 100 °C for 1 h. In particular, the excellent durability of strong acid and alkali resistance, heat resistance, and long-term aging resistance will facilitate the commercial viability and expand the application of SHPL coating in various research fields.

Received 10th May 2023

Accepted 4th July 2023

DOI: 10.1039/d3ra03113f

rsc.li/rsc-advances

1 Introduction

The construction of organic polymer–inorganic hybrid materials at the molecular level or nanoscale can combine the unique properties of organic polymers and inorganic materials at the molecular level.^{1–3} Due to the unique phase structure and a variety of interfacial functional groups in polymers, composite organic polymer–inorganic hybrid materials at the molecular level exhibit unique properties compared with simple hybrid materials.^{4,5} In water dispersion systems, due to their characteristics of long molecular chains, adjustable structure, and easy introduction of polar groups (such as –COOH, –SO₃H and –

NH₂), organic polymer, and inorganic oxide particles can provide steric hindrance and electrostatic repulsion for particles through physical adsorption, thus improving the dispersion and stability of the system.^{6,7} In this context, cross-linking of inorganic NPs with organic polymers has been the focus of attention since 2000.^{8–10}

Due to their large surface area and abundant surface hydroxyl groups, SiO₂ NPs have been used to prepare super/high hydrophilic coatings with surface roughness, which are promising and competitive in a variety of applications, such as solar panels, surface self-cleaning, and anti-fogging glass.^{11–13} However, due to their rich surface activity, they may be dispersed unevenly in the system and easily aggregated, which affects their use.¹⁴ One of the most challenging and advanced issues in all types of hybrids is the pursuit of good functional characteristics such as anti-fogging, transmittance, anti-abrasion, and durability.^{15,16} When heterogeneous components with different transmittance are mixed in the dispersive state, light scattering occurs, which significantly increases the turbidity of the material.^{17–19} Nevertheless, when particles smaller than 20 nm are nano-dispersed in the

^aJiangsu Key Laboratory of Advanced Metallic Materials, School of Materials Science and Engineering, Southeast University, Southeast University Road, Nanjing, 211189, PR China. E-mail: 230228666@seu.edu.cn; yfzhang@seu.edu.cn

^bState Key Laboratory of Advanced Technology for Float Glass, CNBM Research Institute for Advanced Glass Materials Group Co., Ltd, Bengbu 233000, PR China

† Electronic supplementary information (ESI) available. See DOI: <https://doi.org/10.1039/d3ra03113f>



continuous polymer matrix, optically transparent films can be obtained.^{20,21} In this case, the uniform dispersion of NPs in polymer matrices is very difficult because of their large surface area and component incompatibility, which can easily cause polymerization and/or phase separation in the order of tens of nanometers or more.²² Thus, to overcome these problems, several advanced interface designs have been developed using polymerization stabilizers and active surface modifiers.^{23,24} For example, by changing the ratio of comonomers, Zhang *et al.* easily adjusted the interaction between the polymer components (sulfobetaine methacrylate (SBMA) and 2-hydroxyethyl methacrylate (HEMA)) and silica NPs, and prepared coatings with excellent scratch and abrasion resistance.²⁵ Due to the reversibility of the water-assisted electrostatic and hydrogen bond interactions, the coatings were self-healing and maintained good transparency. To eliminate the optical transparent barrier and realize the versatility of hydrophilic coatings, Zhang *et al.* prepared a polyvinyl alcohol (PVA)/SiO₂ coating *via* an ultrasonic enhanced dispersion and immersion-curing process.²⁶ Combined with a bi-component acrylic polyurethane basecoat, the PVA/SiO₂ coating not only possessed anti-fogging, anti-reflection, self-cleaning and underwater anti-fouling properties, but the universality of its substrates was also further extended. However, these polymers could only adhere to particle surfaces through weak physical interactions, such as van der Waals forces, hydrogen bonds, and electrostatic interactions, leading to the formation of non-uniformly dispersed components in the coating system.^{27,28} In particular, the development of robust super-hydrophilic anti-fogging coatings still has not been explored to date. In addition, SHPL coatings usually have very high surface energy, and thus they easily lose their super hydrophilic energy in a hot and humid environment due to the loss of their active groups.^{29–31} Therefore, anti-boiling property must be considered in the design and manufacture of next-generation anti-fogging coatings.

Excitingly, the double cross-linking strategy is an effective alternative for the preparation of durable SHPL anti-fogging coatings. Herein, we propose a low-cost, scalable strategy for manufacturing SHPL anti-fogging coatings with complex and robust structures, where SiO₂ NPs were confined in a water-based solvent to provide appropriate roughness and an SHPL resin was coated as an outer high surface energy layer to enhance the superhydrophilicity of the system. Also, the interfacial interaction between the SiO₂ NPs and the substrate was further enhanced. Subsequently, double cross-linked TEOS was used as a high surface energy coating, and the “adhesive + NP + adhesive” dual cross-linking strategy was used to achieve a strong ultra-hydrophilic surface. The microstructure, chemical compatibility, thermal energy storage properties, long-term properties, thermal stability and anti-fogging performance of the prepared double cross-linking coating were also evaluated in detail. The designed SiO₂-based SHPL anti-fogging coating provides a surface double cross-linking and highly selective enrichment strategy based on PAA and TEOS, which provides a new strategy to realize SHPL anti-fogging properties and reveals the interaction between unique surface properties and superwettability at the macro level.

2 Experimental

2.1 Experimental materials

Deionized water (Nanjing Wanqing Chemical Glass Instrument Co., LTD), anhydrous ethanol (analytical purity, content $\geq 99.7\%$, Sinopmedicine Group Chemical Reagent Co., LTD), silica sol (particle size of 3–10 nm and solid content of 20%, Nanjing Chaorong New Material Technology Co., LTD), alkenyl sulfonate sodium (Nanjing Wanqing Chemical Glass Instrument Co., LTD), sodium hydroxide (ACS, $\geq 95.0\%$, Shanghai McLean Biochemical Technology Co., LTD), tetraethyl orthosilicate (solid content $\geq 28.4\%$, Sinopdrug Group Chemical Reagent Co., LTD), hydrochloric acid (analytical purity, 38%, Shanghai Pilot Chemical Corporation), sulfuric acid (analytical purity, 38%, Shanghai Pilot Chemical Corporation), hydrogen peroxide (ACS, Content 30%), and water-based polyacrylic resin (content 50.0%, Nanjing Wanqing Chemical Glass Instrument Co., LTD).

2.2 Preparation of coating

After early optimization, the organic–inorganic hybrid superhydrophilic anti-fog coating was prepared. The optimized 2.5 g of O-type silica sol was added to 100 g of deionized water, and 300 μL of hydrochloric acid was added to the solution. After stirring well at room temperature, 2–10 g of aqueous polyacrylic resin was added to the solution and stirred well. Then, 0–2 g tetraethyl orthosilicate (TEOS) was added, and 1.6 g sodium alkenyl sulfonate (SDS) was added and stirred at 50 °C for 12 h. Next, the glass was pretreated using Piranha solution (a mixture of concentrated sulfuric acid and 30% hydrogen peroxide), where it was soaked in the solution for 12 h. Subsequently, it was removed and washed three times with deionized water in an ultrasonic cleaner, and finally dried with high-purity nitrogen gas for use. Finally, an organic–inorganic hybrid superhydrophilic anti-fog coating was sprayed on the glass to form a coating. A spray pen with a diameter of 0.3 mm was used to spray 3 mL of anti-fog paint, and the coating was obtained after curing for 24 h at room temperature. A schematic of the detailed manufacturing process is shown in Fig. 1.

2.3 Characterization of coatings

The surface morphology of the coatings was observed *via* field emission scanning electron microscopy (Nova Nano SEM450, Thermo-Fisher) and their surface composition was characterized using the supporting energy spectrum system. The wettability of each coating surface was measured using a video optical contact angle measuring instrument (OCA 15pro, Data-physics, Germany) with 5 μL of water dripped from directly above the sample to the sample surface after 5 s. The wear resistance of the coating was tested using a Taber wear meter (JM-IV, Tianjin Hongjuli Test Equipment Factory). A CS-10F grinding wheel was used and the speed of the abrasion meter was set to 60 rpm. A digital constant temperature heating table (956C, Wuxi Bang Yuan Machinery Co., LTD) and deionized water were used to test the boiling resistance of the coating. The heat resistance and aging resistance of the coating were tested



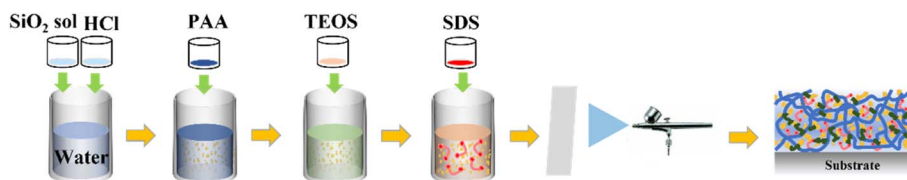


Fig. 1 Schematic of detailed manufacturing process.

using an electric heating air drying oven (DHG-9070, Shanghai Yiheng Scientific Instrument Co., LTD). A solar coating tester (LS182, Shenzhen Linshang Scientific Instrument Co., LTD) was used to measure the optical transmittance of the coating at a specific wavelength of $\lambda = 550$ nm in the visible band of the solar spectrum, which was used to evaluate the anti-fog performance of the coating in its natural state. The adhesion was tested using a pull-out adhesion tester (SZZW-BGD-001, Shenzhen Zhongwei Scientific Instrument Co., LTD). After spraying the coating, the spindle was firmly glued to the surface of the coating with epoxy glue, and then it was placed in a 100 °C oven for 2 h. After the spindle was fixed to the pressure sensor, the drawing test was started. The average of three test results is reported.

3 Results and discussion

3.1 Design strategy and characterization of the composite coating

The molecular weight and viscosity of a polymer solution are two key factors affecting the morphology of crosslinked coatings due to the existence of covalent bonds between the activated glass substrate and the high viscosity and high transparency of water-based organic resins, based on which the adhesion of the coating can be improved and its durability can be guaranteed.^{32,33} In our design, TEOS was used as a double crosslinking binder to further improve the robustness of the coating. Several water-based organic resins (including polyacrylic acid (PAA), polyurethane (PU), epoxy resin A (EP A), epoxy resin B (EP B), polyester resin (PAN), and organic silicon resin (SI)) were selected to optimize the resin. A schematic diagram of the synthetic SiO₂-resin coating is shown in Fig. 2(a). Briefly, using SDS as the stabilizing surfactant, after successively adding resin, deionized water, and nano SiO₂ sol, the organic polymer macromolecules self-assembled around the SiO₂ NPs to obtain SiO₂-resin composite micelles in aqueous solution. It is well known that the adhesion can be further enhanced by adding a hydrophilic resin as an adhesive in the construction of SHPL composite coatings and SiO₂ NPs.³⁴ As shown in Fig. 2(b), compared with the uncoated glass, the WCA of the coated surface was less than 5°, reaching a super hydrophilic state. According to the GB/T 31726-2015 standard, after the slide was placed on a water bath heating device for 60 s, as shown in Fig. 2(c), it still maintained high transparency and no visible fog drops appeared, indicating its excellent anti-fogging property.^{35,36} In addition, the coating had a good appearance. Furthermore, when the coating sample was placed parallel on

colored paper, the image and text below were clearly visible, indicating that the coating has good optical properties. To ensure that the introduction of the resin did not damage the hydrophilic properties of the coating, it was beneficial to construct a hydrophilic resin through screening based on the wettability of the resin. Consequently, the introduction of the optimized resin ensured that the hydrophilicity of the coating was not damaged, contributing to the construction of a super hydrophilic coating. The wettability results are shown in Fig. S1.† PAA and polyurethane resin (PU) had good hydrophilic properties, with a WCA of less than 20°, while other resins had a WCA greater than 60°. According to our previous work, EP B is a fluorocarbon resin with a C-F bond and low surface energy, and thus its intrinsic contact angle is large. In contrast, EP A, PAN, and SI have higher surface energies. However, PU and PAA contain abundant hydrophilic hydroxyl groups.^{30,37} Therefore, PAA and PU were selected as organic components to prepare the organic and inorganic hybrid coatings.

To further study the influence of different components on the surface morphology of the coating, the SEM morphology of the SiO₂ NPs after crosslinking with two types of resins was compared. As shown in Fig. 2(d), the surface of the coating with 0.5 wt% SiO₂ NPs was observed to possess the obvious convex morphology of the NPs, in which the size of the raised NPs was about 3–10 nm. The surface morphology of the initial coating was uniform, and the spherical particles were closely arranged without gaps, holes and other defects. A comparison of the surface morphology of the PU-SiO₂ and PAA-SiO₂ coatings is shown in Fig. 2(e and f), respectively. Meanwhile, a comparison of the surface morphologies of the polyurethane and PAA crosslinking coatings at different magnifications is shown in Fig. S2.† As shown in Fig. 2(e) and S2(a–c),† there is an obvious porous structure on the surface of the PU-SiO₂ coating. At a higher magnification, as shown in Fig. S2(a),† a large number of spherical NPs exposed on the coating surface through these holes can be observed. In contrast, the PAA-SiO₂ coating was more uniform and denser, as shown in Fig. 2(f) and S2(d–f),† indicating that the PAA resin resulted in better encapsulation without significant exposure of the spherical NPs. The surface of the PAA resin became relatively rough, and the SiO₂ NPs were adsorbed on the surface of PAA, indicating the formation of strong interfacial bonding between the organic phase and inorganic phase.³⁸

Considering transparent anti-fogging applications, it was necessary to investigate about optical transparency, surface wettability and abrasion resistance of the coating. As shown in Fig. 2(g and h), the transparency of the SiO₂ coating without



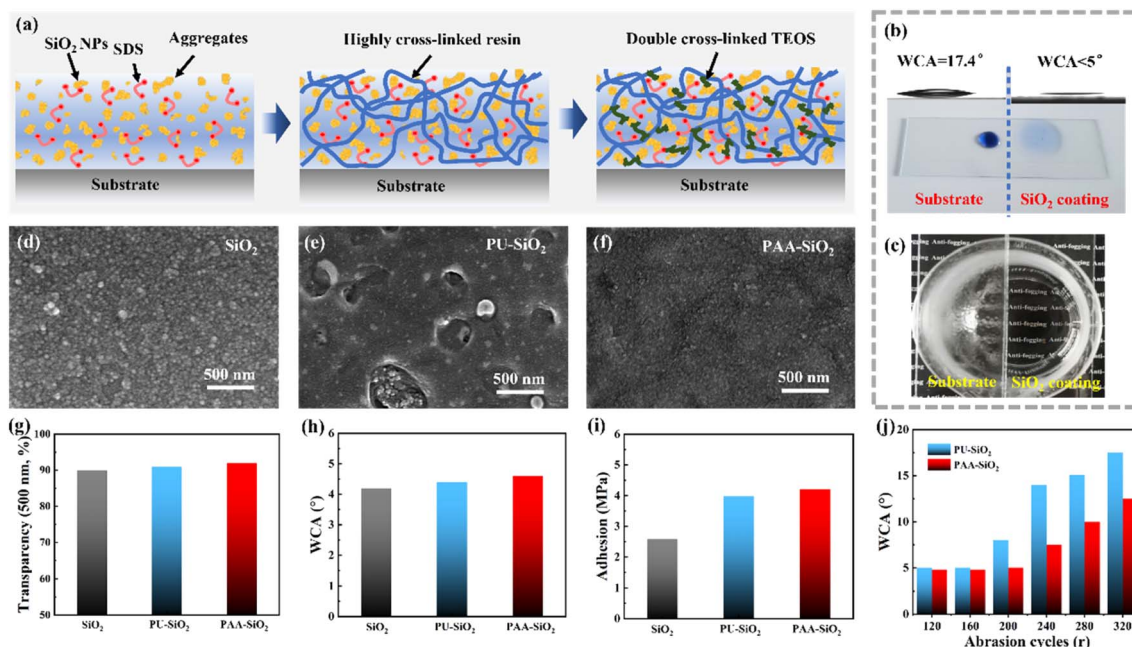


Fig. 2 (a) Schematic diagram of the double cross-linking design of the anti-fogging SHPL coating. (b) Wettability and (c) anti-fogging performance of the glass substrate and SHPL SiO₂ coating. SEM surface images of (d) SiO₂, (e) PU-SiO₂, and (f) PAA-SiO₂ coating. (g) Transparency, (h) WCA, and (i) adhesion on glass of SiO₂, PU-SiO₂, and PAA-SiO₂ coating. (j) WCA of PU-SiO₂ and PAA-SiO₂ coating after different Taber abrasion cycles.

crosslinking remained at 90%. Subsequently, after crosslinking with PU and PAA, the transparency of the coating was 91% and 92%, respectively. Furthermore, droplets (3 μ L) were dropped on the ceramic coating and composite coating, and the average value of the WCA was taken as the WCA of the coating surface. The hydrostatic contact angles of the ceramic coating and composite coating are 4.2°, 4.4° and 4.6°, respectively. The results indicated that the three coatings had a small contact angle, which is consistent with the fact that there are abundant -OH and -COOH hydrophilic groups on the surface of the SiO₂ NPs, PU, and PAA.^{39–41} The adhesion test results of the three coatings are presented in Fig. 2(i), where the adhesion of the inorganic coating without resin is 2.59 MPa. The adhesion of the organic and inorganic hybrid coating with PU resin increased to 3.98 MPa. Meanwhile, the adhesion of the organic and inorganic hybrid coating with PAA resin increased to 4.21 MPa. It can be seen that the prepared PU-SiO₂ coating and PAA-SiO₂ coating had a good appearance and initial anti-fogging performance, and the adhesion between the coating and the substrate also improve. In the case of the abrasion resistance of the PU-SiO₂ coating and PAA-SiO₂ coating, as shown in Fig. 2(j), the abrasion resistance of latter was obviously better. After the 240 r Taber abrasion test, the WCA of the PU-SiO₂ coating was close to 15°, which greatly damaged the superhydrophilicity and anti-fogging effect of the coating. However, under the same condition, the WCA of the PAA-SiO₂ coating was only about 6°, which still maintained a good SHPL and anti-fogging effect (Fig. S3†). Combined with the adhesion comparison results, the surface of the PAA-SiO₂ coating was more uniform and denser than that of the PU-SiO₂ coating, and

thus its strength was relatively higher and it had better abrasion resistance. Therefore, the PAA water-based transparent resin was selected to construct the organic and inorganic hybrid coating.

To further optimize the content of PAA resin to obtain the coating with the best performance, coatings with a PAA content of 1 wt%, 2 wt%, 3 wt% and 4 wt% were prepared, and organic and inorganic hybrid coatings were prepared to study the changes in light transmittance, abrasion resistance and boiling resistance with an increase in the resin content. As mentioned above, the particle size of the NPs in the coating was closely related to its final transmittance.⁴² Therefore, the relationship between particle size and PAA resin content in the coating was quantitatively analyzed using a laser particle size analyzer, and the transparency of the coating was further characterized, as shown in Fig. 3(a). The particle size of the NPs increased with an increase in the content of PAA. The particle size of the coating with 1 wt% PAA was 48 nm, while that of the coating with 2 wt% PAA was 164 nm. When the PPA content was further increased to 3 wt% and 4 wt%, the particle size reached 186 nm and 285 nm, respectively. Thus, it can be concluded that there is a positive correlation between the PAA content and particle size. With an increase in the PAA content, the transparency of the 1 wt%, 2 wt% and 3 wt% coatings corresponded to 91.1%, 90.6% and 90.0%, respectively. Subsequently, with a further increase in the resin content to 4 wt%, the transparency of the coating was significantly reduced to 88.9%, as shown in Fig. 3(b); meanwhile, the actual sample was whiter and foggy than the bare glass slide. On the one hand, the increase in particle size increased the roughness of the coating surface,



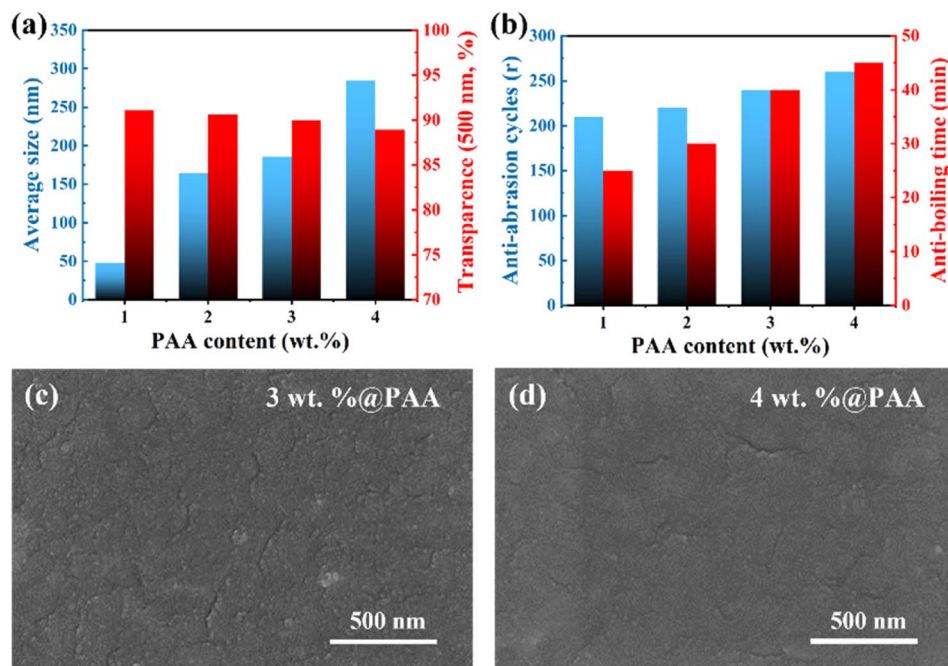


Fig. 3 (a) Average size and transparency of the PAA-SiO₂ SHPL coating at different mass ratios of PAA. (b) Anti-abrasion cycles and anti-boiling time of PAA-SiO₂ coatings at different mass ratios of PAA. SEM surface image of PAA-SiO₂ coating at (c) 3 wt% and (d) 4 wt% PAA mass ratio.

thus enhancing the light scattering effect; on the other hand, it also enhanced the light scattering effect of the particles themselves, and finally the transmittance of the coating decreased significantly.⁴³ Thus, to balance the transmittance and durability of the coating, the organic and inorganic hybrid coating was prepared by mixing 3 wt% PAA resin. Under the condition that the transparency of the coating was maintained at higher than 90%, the results of the Taber abrasion resistance under 250 g load and the boiling resistance test are illustrated in Fig. 3(c). The corresponding abrasion resistance of the coatings with a PAA content of 1 wt%, 2 wt%, 3 wt% and 4 wt% reached 210 r, 220 r, 240 r, and 260 r cycles of abrasion resistance, respectively. Meanwhile, the boiling time of the coatings reached 25 min, 30 min, 40 min and 45 min, respectively. The presence of PAA provided a good protective “armor” for the coating, preventing the penetration, diffusion, migration, and loss of hydrophilic groups in the SHPL coating when contacted with water molecules.⁴⁴ To observe the crosslinking and redispersion effect of the PAA resin on the TEOS-SiO₂ medium, the surface morphology of the PAA resin was measured, as shown in Fig. 3(d). With an increase in PAA content, the coating became denser and the surface particles were completely coated.

To determine the abrasion resistance durability and degradation mechanism of the as-deposited coatings, the coating morphology, anti-fogging performance and composition changes were characterized with respect to time. Fig. 4(a) and S4(a–c)† shows the morphological changes in the PAA hybrid coating at the scratch and the interface between abrasion and non-abrasion during the process of 0–300 r cycles. As shown in Fig. S4(a)†, after 60 r of abrasion, a single scratch was observed to be shallow and narrow, and no obvious scratch marks were

seen in the abrasion area. After 120–180 r, as shown in Fig. S4(b and c)†, an imprint gradually appeared, and the size of a single scratch became wider, but the scratches in the abrasion area were still less in general. After 240 r of abrasion, as shown in Fig. 4(a), an obvious deep scratch could be observed and the appearance of the scratch was clearly visible, but no abrasion phenomenon occurred. After 300 r of abrasion, a significant change with wide and deep scratches appeared on the surface, as shown in Fig. 4(b). There is a significant difference between the scratches and the surrounding morphology. A smooth surface without the presence of SiO₂ NPs indicates that the coating in the worn area was completely damaged.

To analyze the degradation mechanism of the coating after boiling for 40 min, the changes in its surface morphology were observed during the whole process of boiling from 10 min to 50 min. The change in morphology during the boiling process is shown in Fig. 4(c and d) and S4(d–f)†. As shown in Fig. S4(d and e)†, during the first 20 min of boiling, the spherical SiO₂ NPs were gradually exposed, indicating the dissolution of the resin, accompanied by a degradation in the comprehensive performance of the coating. Slight spalling occurred after the coating was boiled for 30–40 min, as shown in Fig. S4(e)† and 4(c), and exposed areas of the substrate on the nanometer scale could be observed. After boiling for 50 min, the coating structure was obviously damaged, and multi-zone and large area spalling occurred (Fig. 4(d)).

The superhydrophilicity of the PAA-SiO₂ coating is mainly attributed to the hydrophilic group of the SDS surfactant. Given that it is a characteristic element, a variation in the content S element corresponds to the loss of SDS. The variation in the characteristic S content on the surface of the coatings at



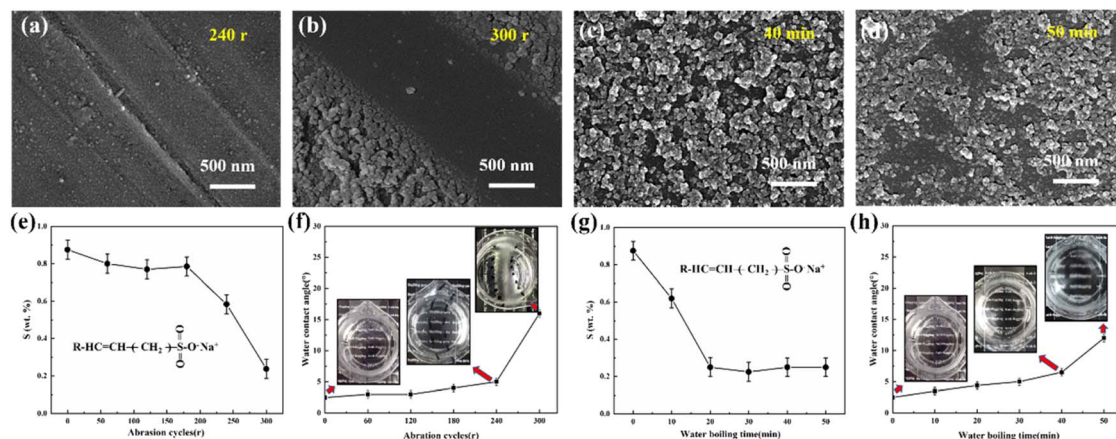


Fig. 4 Surface SEM images of the PAA-SiO₂ coatings after the Taber abrasion test for (a) 240 r cycles and (b) 300 r cycles. Surface SEM images of the PAA-SiO₂ coatings after boiling immersion test for (c) 40 min and (d) 50 min. Change in (e) sulfur content and (f) wettability of surfactant during Taber abrasion test. Change in (g) sulfur content and (h) wettability of surfactant during boiling immersion test.

different stages of abrasion is illustrated in Fig. 4(e). During the abrasion process from 0 to 180 r, the content of S element on the surface of the coating did not decrease significantly compared with the initial stage. Regarding the surface morphology, due to the slight abrasion and good structural integrity at this stage, the surface activity was also completely distributed on the surface of the coating. When the abrasion revolution continued to 240 r, the content of S element decreased to a certain extent, which is consistent with the change in the characteristics of the surface topography of the coating. The surface of the coating worn at 240 r was damaged due to the deep scratches, leading to the loss of hydrophilic substances in a small area. After reaching 300 r, the content of S element decreased significantly, which was only 0.2%. This is because the coating had an obvious spalling phenomenon at this time, which removed a lot of its surface activity, and thus the content of S element on the surface dropped sharply. The WCA and actual anti-fogging effect of the coating at different abrasion stages are shown in Fig. 4(f). Combined with the variation in the surface morphology, chemical composition and actual anti-fogging effect of the coating in the abrasion stage, it can be seen that the coating surface structure was complete within the first 240 r of abrasion, and the hydrophilic substances on the coating surface were also completely distributed, and thus the coating still had a good anti-fogging effect after abrasion. After 300 r of abrasion, the coating structure was obviously damaged, followed by the synchronous loss of hydrophilic substances, and thus the coating degraded with the loss of its anti-fogging effect. The variation in the surface characteristic element S content in the boiling stage of the coating is shown in Fig. 4(g). Different from the morphology, the S element was rapidly lost within 20 min of boiling, where its content decreased from 0.88% to 0.3%. With an increase in the boiling time, and the content of S element remained at about 0.2% and no obvious fluctuation occurred. This is because after boiling for 20 min, most of the hydrophilic substances in the coating were lost to the water environment and formed a dynamic balance, and consequently

the S element on the surface of the coating did not change in the subsequent boiling process. The change in the WCA on the coating surface and the change in the actual anti-fogging effect in the corresponding boiling stage were further characterized, as shown in Fig. 4(h). In the first 40 min of boiling, the WCA of the coating was maintained at less than 6°, which could maintain good superhydrophilicity and anti-fogging performance. After boiling for 50 min, the WCA increased to about 10°, and the anti-fogging effect decreased significantly. Based on the changes in surface morphology, elements and actual anti-fogging effect of the coating during the whole boiling stage, it can be seen that although the hydrophilic components were rapidly lost within the first 40 min of boiling, the structural integrity of the coating was relatively high. This is because the synergistic effect of the hydrophilic substances with the relatively complete surface structure caused the coating to maintain a good super-hydrophilic anti-fogging effect.⁴⁵ However, after boiling for 50 min, the structure of the coating was obviously damaged with a decrease in hydrophilic substance content, and thus the coating degraded and lost its anti-fogging characteristics.

To obtain higher abrasion resistance and boiling resistance, an appropriate amount of TEOS crosslinking agent was added to the hybrid coatings to improve their strength. Based on this strategy, coatings containing 0.5 wt%, 1.0 wt%, 1.5 wt% and 2.0 wt% TEOS were prepared, and their transparency and surface morphology were determined. As shown in Fig. 5(a–d), with an increase in TEOS content, the coating gradually presented a dense network structure. In addition, as shown in Fig. 5(e), the increase in TEOS content has no significant effect on the transmittance of the coating. To further understand the effect of microstructure changes on the coating properties, the wettability of five coatings after boiling for 60 min was tested to measure the boiling resistance of each coating. As shown in Fig. 5(f), with an increase in TEOS content, the WCA of the coating gradually decreased after boiling for 60 min. When the TEOS increased to 1.5 wt%, the WCA of the coating after boiling



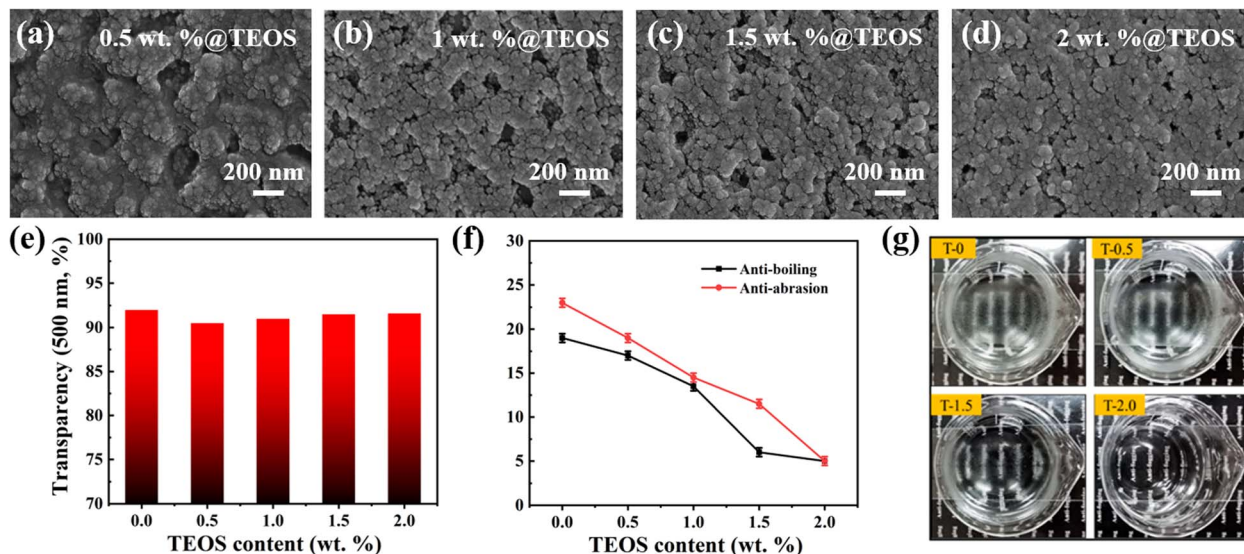


Fig. 5 Surface SEM images of the PAA-TEOS-SiO₂ coating with different mass ratios of TEOS: (a) 0.5 wt%, (b) 1 wt%, (c) 1.5 wt%, and (d) 2 wt%. (e) Transparency of the PAA-TEOS-SiO₂ coating with different TEOS contents. (f) Wettability changes after anti-boiling and anti-abrasion tests and (g) anti-fogging performance of the PAA-TEOS-SiO₂ coating with different TEOS contents.

for 60 min was about 5°, which had a good actual anti-fogging effect. With different TEOS contents in the coating and after 300 r of abrasion test, the change in actual anti-fogging effect is illustrated in Fig. 5(g). After boiling at 60 °C for 1 h, the coating with a TEOS content of 2 wt% could maintain a good anti-fogging performance.

To explore the reasons for the enhanced durability, the micro-morphologies of the coatings were compared and observed after 300 r of abrasion and 60 min of boiling. As shown in Fig. 6(a₁), when the TEOS content was 0.5 wt% or less, the hybrid coating was seriously damaged after 300 r of abrasion, forming scratches about 1–2 μm wide, and the scratches were obviously worn and almost no SiO₂ NPs existed. With an increase in TEOS content to 1–1.5 wt%, no clear scratch edge was seen, and nanoparticles were observed in the scratch and not completely worn through (Fig. 6(a₂ and a₃)). As shown in Fig. 6(a₄), for the coating with a TEOS content of 2 wt%, only blots were visible without obvious abrasion, and the SiO₂ NPs in the scratches were only flattened without peeling off. These results proved that with an increase in the TEOS content, the abrasion resistance of the coating gradually increased, and the coating with 2 wt% TEOS content could still maintain a relatively complete structure after 300 r of abrasion. Meanwhile, compared with similar SiO₂-based SHPL coatings (Table S1†), the current work shows good abrasion resistance.

A comparison of the surface morphology of each coating after 60 min of boiling process is shown in Fig. 6(b₁–b₄). When the TEOS content was 0.5–1.0 wt%, the coating could be evenly peeled off after boiling, and the peeling area gradually decreased with an increase in TEOS content (Fig. 6(b₁ and b₂)). Combined with the initial morphology of the coating, it can be seen that the exfoliation resulted in some large-sized SiO₂ NPs aggregating in the coating. Due to their small specific surface area, the binding force of the large NPs on the surrounding NPs

and the matrix was weakened. As shown in Fig. 6(b₃ and b₄), when the content of TEOS increased to 1.5–2.0 wt% or above, the difference between the coating morphology and the initial surface morphology after boiling was small, and there was almost no exposed substrate. The results show that with an increase in TEOS content, the degree of crosslinking of the coating improved, and the coating had higher structural stability. To further understand the influence of the micro-structure changes on the coating performance, the wettability of five coatings was tested. By comparing Fig. 6(c) and (e), with an increase in TEOS content to 2.0 wt%, the WCA of the coating could be maintained at about 5° after 60 min of boiling and 300 r of abrasion, proving that improved durability was obtained. The variations in the characteristic S content on the surface of the coatings at different stages of anti-abrasion and anti-boiling tests are illustrated in Fig. 6(d) and (f), respectively. After 300 r and 60 min, the content of S element decreased to about 0.2%. Under the external force of abrasion and boiling, good structural integrity could be maintained for a longer time, thus improving the durability of the coating.

Based on the above-mentioned results and discussion, the enhanced comprehensive performance of double cross-linking can be illustrated by the hydrolysis of PAA and TEOS, including different bonding cases such as electrostatic interaction between SiO₂ NPs and SDS, and covalent bonding between the active glass substrate and PAA. A schematic illustration of the structure of the SiO₂-PAA-TEOS coating is shown in Fig. 7(a). By controlling the pH value of the solution and the electrostatic interaction between the anionic polymer chains, a series of anionic polymers was dispersed in SiO₂ solution on the nanoscale, and transparent and homogeneous SiO₂-PAA-TEOS double-cross-linked materials were synthesized. The phase separation in the system was reduced by controlling the degree of hydrolysis of TEOS, slowing down the condensation of

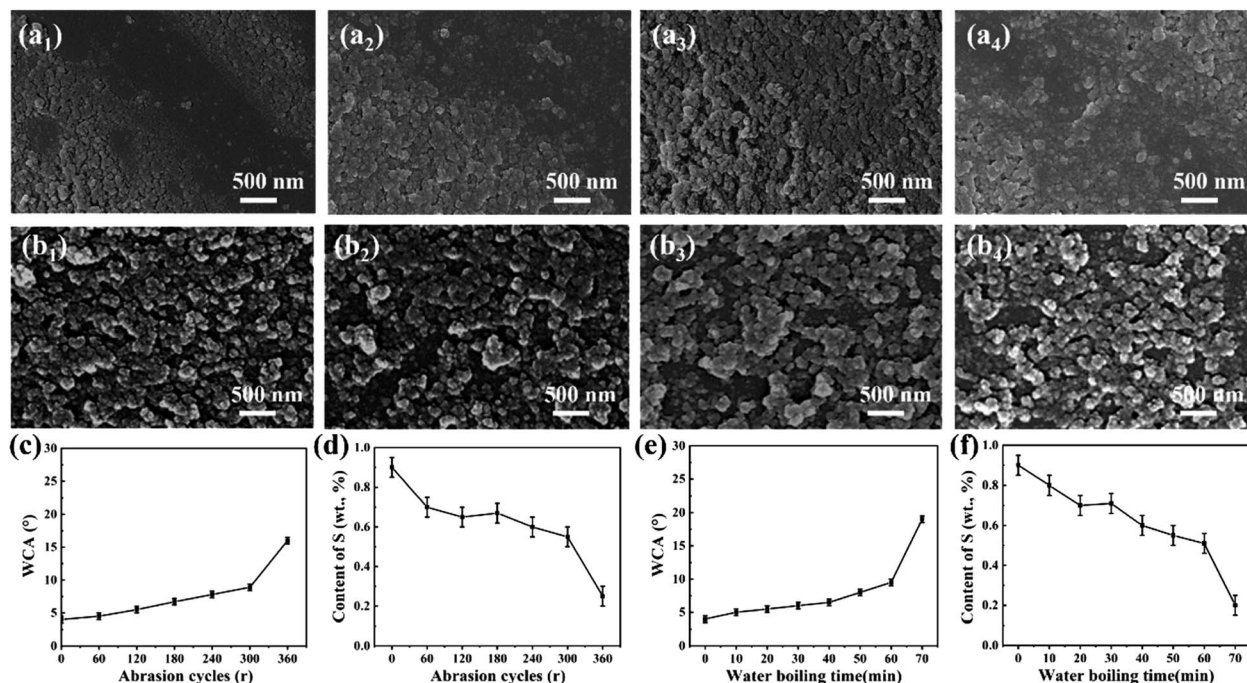


Fig. 6 Surface SEM images of the PAA-TEOS-SiO₂ coating after the Taber abrasion test for 300 r cycles with different mass ratios of TEOS: (a₁) 0.5 wt%, (a₂) 1 wt%, (a₃) 1.5 wt%, and (a₄) 2 wt%. Surface SEM images of the PAA-TEOS-SiO₂ coating after boiling immersion test for 60 min with different mass ratios of TEOS: (b₁) 0.5 wt%, (b₂) 1 wt%, (b₃) 1.5 wt%, and (b₄) 2 wt%. Change in (c) wettability and (d) sulfur content of the surfactant during the Taber abrasion test. Change in (e) wettability and (f) sulfur content of surfactant during boiling immersion test.

silanol and introducing coupling sites between the silicon phase and polymer chain in the in crosslinking process instead of using coupling agents. Specifically, the extent to which TEOS hydrolyzed was controlled by the limited availability of water

released during the formation of PAA prior to mixing with the silica solution, which should be nearly the same for all the solutions studied. Therefore, the more TEOS in the starting material, the lower the degree of hydrolysis. In addition, the

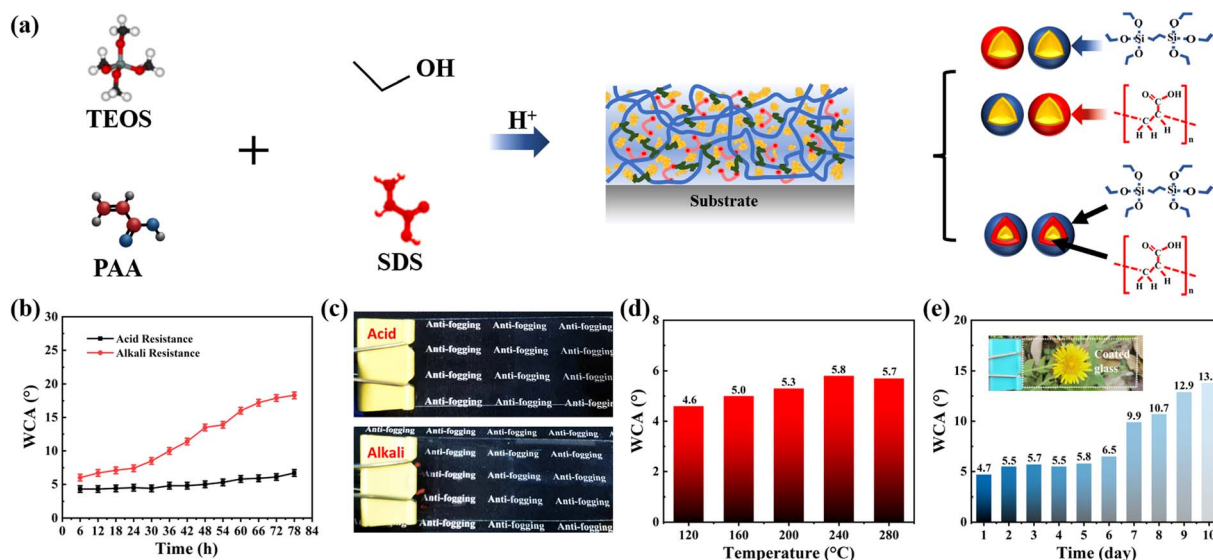


Fig. 7 (a) Schematic diagram of the double cross-linking mechanism of the PAA-TEOS-SiO₂ coating. (b) WCA of the SHPL coating after immersion in 1 M acid solution and 1 M alkali solution for different times. (c) Optical pictures of SHPL coating after immersion in 1 M acid solution and 1 M alkali solution for 36 h and 72 h, respectively. (d) WCA of SHPL coating after heating resistance test at 120 °C, 160 °C, 200 °C, 240 °C, 280 °C for 1.5 h. (e) Aging resistance of organic and inorganic hybrid super hydrophilic anti-fog coating. Inset is a photo of the appearance of the coating after 50 days of aging resistance test.



water released during the dehydration of PAA may also be involved in hydrolysis. It has been mentioned in the literature that due to the direct chemical bonding between the silyl alcohol group and the carboxylic acid group, the carboxylic group of PAA will act as the coupling site between the polymer and the silica phase.⁴⁶ To understand the process for the formation of the SiO₂-PAA-TEOS coating, FT-IR spectroscopy was performed. As shown in Fig. S5,[†] the peaks at 1107 cm⁻¹, 967 cm⁻¹, 796 cm⁻¹, and 1096 cm⁻¹ are attributed to the bending vibration of Si–O, symmetric stretching vibration of Si–O, bending vibration of Si–OH, and asymmetric stretching vibration of Si–O–Si, respectively. The peak at 1727 cm⁻¹ is assigned to the stretching vibration of C=O of the PAA resins. Compared with that of the SiO₂-PAA coating, a new absorption peak at around 1000 cm⁻¹ could be observed for the SiO₂-PAA-TEOS coating, which is assigned to the stretching vibration of the C=O group. This shows that the carboxyl group (–COOH) in the hydrolysis process is cross-linked again with the hydroxyl group (–OH) in the silica phase.³⁰ Thus, the slow polycondensation of the silica phase occurs simultaneously with hydrolyzation, inhibiting the growth of large SiO₂ particles, preventing their agglomeration and increasing the compatibility between the polymer and inorganic phases. Using the above-mentioned three raw materials as the main components, the SHPL anti-fogging coating was prepared *via* the spray method.

To study the decay resistance of the organic and inorganic hybrid SHPL coating, the above-mentioned optimized organic and inorganic hybrid coating was immersed in hydrochloric acid solution with pH = 2 and sodium hydroxide solution with pH = 13, the acid and alkaline resistance of the coating was tested, and the change in the WCA on the coating surface after soaking for different times was recorded. As shown in Fig. 7(b), the WCA of the coating remained below 6° after soaking in sodium hydroxide solution for 18 h, while that of the coating remained about 6° after soaking in hydrochloric acid solution for 72 h. The coating had good acid resistance and it possessed better acid resistance than alkaline resistance, which can be attributed to the acidic environment during solution preparation, while it was susceptible to oxidative degradation in alkaline environments. However, as shown in Fig. 7(c), after the alkaline resistance test, the SiO₂-PAA-TEOS coating did not show bleaching phenomenon compared with the SiO₂ inorganic coating, which indicates that the acid and alkali resistance further improved. Therefore, the addition of resin and the improvement in stable structure are beneficial for the construction of coatings with anti-oxidation and decomposition properties, thereby improving their acid and alkaline resistance.

An accelerated aging experiment was performed to test the aging resistance. Specifically, the coating was stored at 180 °C, and the wettability of the coating surface was measured and recorded every 5 days. As shown in Fig. 7(d), after 25 days of aging resistance test, the coating still maintained an SHPL state with a WCA of <6°. After 50 days of aging resistance test, the WCA increased to 13.8° with no changes in its appearance such as the appearance of yellow and spots on its surface. Also, the

slight increase in WCA can be attributed to the oxidative decomposition at high temperature for the organic PAA resin with carbon chains as a skeleton. Therefore, the coatings containing resins were often more sensitive to temperature and more likely to degrade under continuous high temperature treatment. To test the heat resistance, the coating was placed at different temperatures for 90 min, then cooled naturally to room temperature, and its surface WCA measured, as shown in Fig. 7(e). After thermal treatment at 120 °C, 160 °C, 200 °C, 240 °C and 280 °C, the WCA of the coating was less than 6°. The results show that the coating has good aging and heat resistance and it maintained its SHPL and anti-fogging properties in the temperature range of 0–280 °C.

4 Conclusions

By selecting different hydrophilic resins and further optimizing the TEOS content, the dual cross-linking of SiO₂ NPs was achieved, and a transparent, SHPL, and durable anti-fogging coating was obtained *via* a simple universal spraying method. The repulsion between SiO₂ in the sol solution and its low permeability threshold led to the formation of a fractal nanoporous inorganic surface, while the optimized hydrophilic PAA resin acted both as a surface modifier for the NPs and a chemical binder between the substrates and NPs as well as between the NPs. By adjusting the content of TEOS in the coating, its compact surface structure contributed to higher durability. The prepared SHPL anti-fogging PAA-TEOS-SiO₂ coatings exhibited good corrosion resistance, water resistance and abrasion resistance, high temperature thermal stability, and could maintain their superhydrophilicity after treatment at 180 °C for 25 days. The unique design of double cross-linking of SiO₂ NPs and two organic solvents, as well as the investigation of individual effects to achieve high transparency and SHPL anti-fogging properties will provide new insights into how to design scalable coatings for nanofabrication with enhanced durability.

Author contributions

Xingyu Liu and Lili Xu contributed equally to this work. Xingyu Liu: conceptualization, investigation, methodology, writing – original draft. Lili Xu: methodology, validation, conceptualization, theoretical analysis. Shuaisheng Zhao: investigation, validation, methodology, writing – review & editing. Haoxuan Hua: investigation. Zhiping Gan: investigation. Jinlei Wang: investigation. Yifan Su: investigation. Xinquan Yu: funding acquisition, review & editing. Youfa Zhang: project administration, supervision, review & editing.

Conflicts of interest

The authors declare no conflict of interest.



Acknowledgements

The authors gratefully acknowledge the financial support from the National Natural Science Foundation of China (Grants 52071076) and Opening Project of State Key Laboratory of Advanced Technology for Float Glass (Grants 2022KF03).

References

- 1 S. Yamamoto and H. Kai, *Adv. Mater. Interfaces*, 2022, **9**, 2201736.
- 2 J. Choi, C. Lee, J. Kang, C. Lee, S. M. Lee, J. Oh, S. Y. Choi and S. G. Im, *Small*, 2022, **18**, e2203165.
- 3 B. H. Kwon, C. W. Joo, H. Cho, C. M. Kang, J. H. Yang, J. W. Shin, G. H. Kim, S. Choi, S. Nam, K. Kim, C. W. Byun, N. S. Cho and S. Kim, *ACS Appl. Mater. Interfaces*, 2021, **13**, 55391–55402.
- 4 Y. Tang, Y. Li, Y. Zhang, C. Mu, J. Zhou, W. Zhang and B. Shi, *Ind. Eng. Chem. Res.*, 2020, **59**, 3383–3393.
- 5 T. Li, Y. Wang, X. Liu, S. Yang, S. Zhang, S. Wang and W. Dong, *ACS Appl. Polym. Mater.*, 2022, **4**, 8147–8155.
- 6 B. Yang, Y. Zhou, W. Yu, S. Zhang, H. Chen and J. Ye, *Polym. Int.*, 2019, **68**, 675–683.
- 7 M. Yu, S. Zhao, L. Yang, N. Ji, Y. Wang, L. Xiong and Q. Sun, *Carbohydr. Polym.*, 2021, **271**, 118422.
- 8 Q. Yu, Y. Yin, Y. Yang, Y. Han, Y. Liu, B. Li and L. Weng, *J. Sol-Gel Sci. Technol.*, 2018, **87**, 749–759.
- 9 A. Li, Y. Jia, S. Sun, Y. Xu, B. B. Minsky, M. A. C. Stuart, H. Colfen, R. von Klitzing and X. Guo, *ACS Appl. Mater. Interfaces*, 2018, **10**, 10471–10479.
- 10 Y. Li, L. Cai, X. Zhang, Y. Chen, Z. Cui, J. Luo, J. Li, J. Li, S. Q. Shi and Q. Gao, *J. Cleaner Prod.*, 2023, **400**, 136730.
- 11 A. Sriboonruang, T. Kumpika, E. Kantarak, W. Sroila, P. Singjai, N. Lawan, S. Muangpil and W. Thongsuwan, *Chiang Mai J. Sci.*, 2020, **47**, 823–828.
- 12 P. Chen, Y. Hu and C. Wei, *Appl. Surf. Sci.*, 2012, **258**, 4334–4338.
- 13 W. Xinying, X. Peng, X. Mingbiao, P. Lei and Z. Yu, *Arabian J. Chem.*, 2023, **16**, 104394.
- 14 J. Cui, Z. Zhou, A. Xie, M. Meng, Y. Cui, S. Liu, J. Lu, S. Zhou, Y. Yan and H. Dong, *Sep. Purif. Technol.*, 2019, **209**, 434–442.
- 15 E. Nam, E. H. H. Wong, S. Tan, Q. Fu, A. Blencowe and G. G. Qiao, *Macromol. Mater. Eng.*, 2017, **302**, 1600199.
- 16 Y. Wang, J. Knapp, A. Legere, J. Raney and L. Li, *RSC Adv.*, 2015, **5**, 30570–30576.
- 17 J. A. Howarter and J. P. Youngblood, *Macromol. Rapid Commun.*, 2008, **29**, 455–466.
- 18 H. Lee, M. L. Alcaraz, M. F. Rubner and R. E. Cohen, *ACS Nano*, 2013, **7**, 2172–2185.
- 19 S. H. Lee, M. Kang, H. Jang, S. Kondaveeti, K. Sun, S. Kim, H. H. Park and H. E. Jeong, *ACS Appl. Mater. Interfaces*, 2022, **14**, 39478–39488.
- 20 L. Chen, Z. Li, P. Zhang, P. Tian, J. Yuan and W. Zheng, *Ceram. Int.*, 2023, **49**, 6805–6810.
- 21 I. Haechler, N. Ferru, G. Schnoering, E. Mitridis, T. M. Schutzius and D. Poulikakos, *Nat. Nanotechnol.*, 2023, **18**, 137–144.
- 22 M. C. Prete and C. R. T. Tarley, *Chem. Eng. J.*, 2019, **367**, 102–114.
- 23 M. Choi, L. Xiangde, J. Park, D. Choi, J. Heo, M. Chang, C. Lee and J. Hong, *Chem. Eng. J.*, 2017, **309**, 463–470.
- 24 T. Yuan, J. Yin, Y. Liu, W. Tu and Z. Yang, *Polymers*, 2020, **12**, 1378.
- 25 B. Liang, Z. Zhong, E. Jia, G. Zhang and Z. Su, *ACS Appl. Mater. Interfaces*, 2019, **11**, 30300–30307.
- 26 X. Zhang and J. He, *Chem. Commun.*, 2015, **51**, 12661–12664.
- 27 B. Yan, Y. Zhao and Y. J. Li, *Photochem. Photobiol.*, 2011, **87**, 757–765.
- 28 T. Mishra, P. Mandal, A. K. Rout and D. Sahoo, *Compos., Part C: Open Access*, 2022, **9**, 100298.
- 29 M. W. England, T. Sato, C. Urata, L. Wang and A. Hozumi, *J. Colloid Interface Sci.*, 2017, **505**, 566–576.
- 30 W. Deng, Y. Su, C. Zhang, W. Wang, L. Xu, P. Liu, J. Wang, X. Yu and Y. Zhang, *J. Colloid Interface Sci.*, 2023, **642**, 255–263.
- 31 M. Liu, M. Zhao, S. Yang, Y. Zhang, Y. Zhou and J. Zhang, *Prog. Org. Coat.*, 2023, **182**, 107601.
- 32 H. Liu, H. Yu, X. Yuan, W. Ding, Y. Li and J. Wang, *Chem. Eng. J.*, 2019, **374**, 1394–1402.
- 33 S. Cheng, D. Shen, X. Zhu, X. Tian, D. Zhou and L.-J. Fan, *Eur. Polym. J.*, 2009, **45**, 2767–2778.
- 34 P. Lu, J. Xu, W. Tian, C. Zhang, S. Niu, J. Zhao, W. Ming and L. Ren, *Chem. Eng. J.*, 2023, **465**, 142868.
- 35 GB/T 31726-2015, 2015.
- 36 S. Kim and J. H. Park, *ACS Appl. Mater. Interfaces*, 2020, **12**, 42109–42118.
- 37 W. Gu, W. Wang, X. Jiao, W. Deng, Y. Xia, X. Yu and Y. Zhang, *RSC Adv.*, 2022, **12**, 16510–16516.
- 38 F. Meng, Y. Xu, Z. Wu and H. Chen, *Compos., Part C: Open Access*, 2022, **642**, 128724.
- 39 R. S. Sutar, P. B. Patil, A. K. Bhosale, S. Nagappan, S. R. Shinde, P. P. Chikode, C. E. Patil, S. S. Kadam, P. M. Kadam, C. R. Bobade, K. K. Sadasivuni, K. H. Park and S. S. Latthe, *Macromol. Symp.*, 2021, **400**, 2100083.
- 40 S. Chen, S. Li, Z. Ye, Y. Zhang, S. Gao, H. Rong, J. Zhang, L. Deng and A. Dong, *Chem. Eng. J.*, 2022, **446**, 136985.
- 41 T. Han, Z. Ma and D. Wang, *ACS Macro Lett.*, 2021, **10**, 354–358.
- 42 J. Y. Seo and M. Han, *Nanotechnology*, 2011, **22**, 025601.
- 43 A. Seifi, D. Salari, A. Khataee, B. Çoşut, L. Ç. Arslan and A. Niaei, *Ceram. Int.*, 2023, **49**, 1678–1689.
- 44 L. Chen, L. Li, L. Zhang, S. Xing, T. Wang, Y. A. Wang, C. Wang and Z. Su, *ACS Appl. Mater. Interfaces*, 2013, **5**, 7282–7290.
- 45 Y. Zhang, S. Zhang and S. Wu, *Chem. Eng. J.*, 2019, **371**, 609–617.
- 46 R. Aghaei and A. Eshaghi, *J. Alloys Compd.*, 2017, **699**, 112–118.

